



HAL
open science

Mass log-stable distribution of fragments in liquid–liquid jet fragmentation based on a two-step cascade between viscous Kelvin-Helmholtz instability and Rayleigh-Taylor instability

Nicolas Rimbert, Miloud Hadj-Achour, Bowen Ji, Gagan Kewalramani, Alexandre Labergue, Yvan Dossmann, Michel Gradeck, Pascal Piluso, Renaud Meignen

► To cite this version:

Nicolas Rimbert, Miloud Hadj-Achour, Bowen Ji, Gagan Kewalramani, Alexandre Labergue, et al.. Mass log-stable distribution of fragments in liquid–liquid jet fragmentation based on a two-step cascade between viscous Kelvin-Helmholtz instability and Rayleigh-Taylor instability. *International Journal of Multiphase Flow*, 2023, 167, pp.104518. 10.1016/j.ijmultiphaseflow.2023.104518 . hal-04151013

HAL Id: hal-04151013

<https://hal.univ-lorraine.fr/hal-04151013>

Submitted on 18 Aug 2023

HAL is a multi-disciplinary open access archive for the deposit and dissemination of scientific research documents, whether they are published or not. The documents may come from teaching and research institutions in France or abroad, or from public or private research centers.

L'archive ouverte pluridisciplinaire **HAL**, est destinée au dépôt et à la diffusion de documents scientifiques de niveau recherche, publiés ou non, émanant des établissements d'enseignement et de recherche français ou étrangers, des laboratoires publics ou privés.



Distributed under a Creative Commons Attribution - NonCommercial - NoDerivatives 4.0 International License

Mass log-stable distribution of fragments in liquid-liquid jet fragmentation based on a two-step cascade between viscous Kelvin-Helmholtz instability and Rayleigh-Taylor instability

Nicolas Rimbart^a, Miloud Hadj-Achour^a, Bowen Ji^a, Gagan Kewalramani^a,
Alexandre Labergue^a, Yvan Dossmann^a, Michel Gradeck^a, Pascal Piluso^b,
Renaud Meignen^c

^a*LEMETA CNRS Universite de Lorraine Vandoeuvre-les-Nancy 54518 France*

^b*CEA DES\IRESNE\DTN\SMETA\LEAG Cadarache France*

^c*Institut de Radioprotection et de Surete Nucleaire (IRSN) Saint Paul Lez Durance France*

Abstract

This work is devoted to the study of liquid-liquid fragmentation. It contains both an experimental part and a theoretical part. In the experimental part, a low-melting point liquid metal jet is injected into a water pool. High-speed shadowgraph method is used to measure the jet velocity and to observe the dynamics of the fragmentation. Thereafter, the solidified fragments are sieved and weighted allowing to measure their mass distribution according to their size. The mass Probability Density Function (PDF) is then fitted using log-stable laws, generalization of log-normal laws. In the theoretical part, it is shown how it is possible to compute the shift parameter of the stable law considering that the droplet are mainly generated by a boundary layer stripping mechanism. Actually the computation relies on a viscous Kelvin-Helmholtz instability mechanism sometime called "gradient instability". The width of the distribution (or more precisely its scale parameter) is computed assuming a cascade mechanism between this first wave instability and a secondary Rayleigh-Taylor mechanism. The model is then compared to present experimental results and previously published results obtained in the field of nuclear safety studies (Fuel-Coolant Interaction or FCI). Two fitting parameters are then identified. The agreement is good when phase change and solidification effects can be neglected and qual-

itatively good (*i.e.* fitting parameters need to be modified) when these effects cannot be neglected.

Keywords: `elsarticle.cls`, L^AT_EX, Elsevier, template

2010 MSC: 00-01, 99-00

1. Introduction

Atomization and Sprays have a wide range of applications and are now a common field of study in multiphase flow. The present paper is dedicated to the study of liquid-liquid jet fragmentation with high density ratio. The main
5 motivation of this work is related to the understanding and modeling of the the premixing stage of "Fuel-Coolant Interaction" (FCI) in the frame of severe accident in Nuclear Power Plants. This situation involves the mixing of the hot molten core (corium) interacting with surrounding cooling water. The "cold" configuration, that is presented here, cannot really be representative of the
10 real situation where the melt reaches temperatures between 2000 and 3000 K (depending on its composition: U-Zr-Fe-O and various fission products), and thus yields an important vapor production (as well as H_2 production due to oxidation). Nevertheless, in order to be able to produce adequate modeling in the 3-phase situation, it is necessary to better understand and model the
15 simpler situations of liquid/liquid and liquid/gas configuration. The present study is therefore devoted to the liquid/liquid case, which have been much less studied than the liquid/gas one but may bear similar mechanisms.

In the present work, overheating of the molten metal is low enough so that no vapour is ever produced. This allows using non-intrusive optical diagnostics
20 like high-speed shadowgraphy in order to build models that could eventually be used on more realistic case (comparison will be made with previously published results). A traditional sieving methods is also employed to analyse the debris. To do so, the water temperature has been chosen so that the melt could solidify only once the fragmentation process is complete.

25 As liquid/liquid is expected to bear similarity with liquid/gas case, let us re-

call that recent advances concerns firstly the influence of intermediate ligament in the fragmentation process [1], (though not really new, see [2] for instance). The main result of the authors, here, is that ligament breakup dynamics lead to a Gamma distribution of the daughter droplets. However, no leads to how-to
30 compute parameters of the Gamma distribution has been found in the general case up to now. Furthermore, this result seems to contradict Kolmogorov analysis [3], leading to log-normal distribution, recently modernized [4, 5, 6, 7]. Even in the Kolmogorov frame of analysis, the computation of the parameters in the general case is still difficult though some few models do exist [8]. Last, com-
35 petition between classical instabilities such as Rayleigh-Taylor instability (often associated to bag-breakup) or Kelvin-Helmholtz instabilities (often associated to boundary layer stripping) is known to be fundamental in the modelling. This leads to semi-empirical models such as the so-called WAVE model [9, 10] which are still used nowadays in commercial Computer Fluid Dynamics codes. Exper-
40 imental results have also shown the importance of using a cascade of instability (Rayleigh-Taylor building up on Kelvin-Helmholtz wave) in the case of an airblast atomizer [11].

In the wake of these works, Rimbert & Séro-Guillaume [6] developed an extension of Kolmogorov's work to log-stable law and applied it successfully to
45 high-Weber number (third party) spray Mass Probability Distribution Function (PDF). These laws are generalizations of log-normal laws and are sometimes known as universal multifractals [12, 13]. However, in this first work, the parameters were fitted and no phenomenological explanation about their value was given. Building on Kida's work [14, 15], Rimbert [16] gave a possible explana-
50 tion (self-avoiding vortex tangles related to angular momentum conservation) of the importance of log-stable law in the modelling of fine-scale structure of turbulence, but most importantly, also gave a way to compute the stability index α of the distribution ($\alpha \approx 1.7$).

Liquid-liquid studies are comparatively scarcer (*cf.* [17, 18, 19, 20, 21, 22, 23,
55 24, 25] for instance) and mainly focus on severe nuclear accidents (with vapor production) and granulometry of the fragments (using mainly the Mass Median

Diameter or MMD). The modelling is focused on comparing these MMD to either classical Kelvin-Helmholtz or Rayleigh-Taylor wavelengths. Moreover, the mass PDF is seldom reported precisely (*i.e.* in a table). The purpose of present work is to show how mass log-stable distribution [6] allows for the computation of the droplet PDF in present liquid-liquid case. The Mass PDF is found to be mainly driven by large scale instabilities in a successive manner, hereafter named "two-step cascade": first a viscous boundary layer wave instability [26] then more classically a Rayleigh-Taylor instability; however appearing in a subsequent cascading step (*i.e.* the corresponding length scales are computed using the length scale generated by the first instability). It will also be shown how to compute all the relevant parameters of the distributions using the proposed phenomenology. Lastly, comparison with previously cited liquid/liquid experiments will be made whenever possible.

2. Experimental set-up

2.1. Non dimensional numbers

The four non dimensional parameters governing the hydrodynamics of the fragmentation of a liquid jet of diameter D_0 and velocity U_0 are: the (carrier) Weber number We , the Ohnesorge number Oh ,

$$We = We_C = \frac{\rho_C U_0^2 D_0}{\gamma}, \quad Oh = \frac{\mu_L}{\sqrt{D_0 \rho_L \gamma}}, \quad (1)$$

the density ratio ρ_R and the viscosity ratio μ_R , where subscript L refers to the properties of the Liquid jet and subscript C refers to the properties of the Carrier phase.

$$\rho_R = \frac{\rho_L}{\rho_C}, \quad \mu_R = \frac{\mu_L}{\mu_C} \quad (2)$$

In the present case, the Weber number is the main hydrodynamic parameter. Other important non dimensional parameters will be used, they are: the Reynolds numbers (for the carrier and the liquid)

$$Re_C = \frac{\rho_C U_0 D_0}{\mu_C}, \quad Re_L = \frac{\rho_L U_0 D_0}{\mu_L} \quad (3)$$

and the liquid Weber number

$$We_L = \frac{\rho_L U_0^2 D_0}{\gamma}. \quad (4)$$

Note that $Oh = \sqrt{We_L}/Re_L$.

2.2. Set-up description

The experimental set-up is a modification of the drop-on-demand set-up
 85 used in Hadj-Achour *et al.* [27], himself derived from Amirzadeh *et al.* [28].
 The liquid metal injector is represented on figures 1 and 2. It uses Field's
 metal, a eutectic alloy of Tin, Bismuth and Indium, whose melting temperature
 is 62°C. The temperature of the melt (85°C) is kept by a double-boiler ("bain-
 marie") technique. Table 1 gives the physical properties of Field's metal that
 90 have been previously measured [27] and are used in present analysis to compute
 the aforementioned non dimensional numbers.

ρ	γ	k	μ	L_f	C_p
kg/m ³	N/m	$\frac{W}{m.K}$	Pa.s	$\frac{J}{kg}$	$\frac{J}{kg.K}$
7994	0.41	5.44	0.01	26415	300

Table 1: Physical Properties of Field's metal. ρ is the density, σ is the water/liquid metal interfacial tension, k is the thermal conductivity, μ is the dynamic viscosity, L_f the fusion latent heat and C_p the heat capacity.

The GaLaD (for "Goutte à La Demande" *i.e.* Drop-On-Demand) experi-
 mental setup (*cf.* figure 1) has been modified to include an electro-magnet (*cf.*
 figure 2) that allows for the opening of the stem-valve for a longer time thereby
 95 generating a jet (henceforth named JaLaD for "Jet à La Demande" *i.e.* Jet-On-
 Demand). The velocity of the jet is controlled by varying the pressure of the
 Nitrogen gas-supply. A sketch of the experimental set-up is shown on figure 3.

The size of the water pool is 50cm × 50cm × 40cm and is heated to 40°C.
 This choice stems from the initial liquid metal temperature set to 85 °C. To
 100 limit solidification impact during fragmentation, the pool temperature has to
 be increased up to the limit where droplets are still liquid when they touch

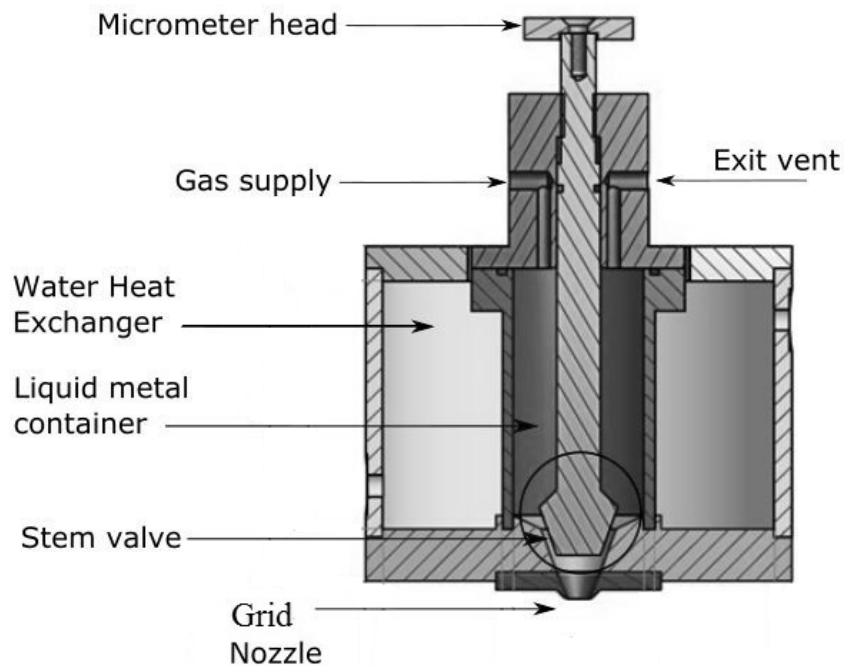


Figure 1: GaLaD experimental Set-up.

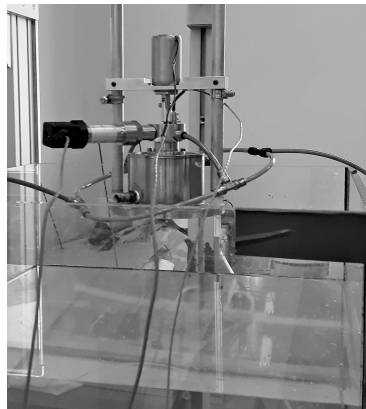


Figure 2: JaLaD experimental Set-up.

the bottom, estimated, empirically, to be 50 °C. This corresponds to a contact temperature T_C of 75 °C, obtained by the following equation (neglecting convection),

$$T_C = \frac{E_L T_L + E_C T_C}{E_L + E_C} \quad (5)$$

105 where E_L and E_C are respectively the thermal effusivity ($\sqrt{k\rho C_p}$) of the Field's metal liquid droplet and ambient carrying water, T_C is the ambient carrying water pool temperature and T_L is the Field's metal liquid droplet temperature. Therefore a lower value, of 40 °C, has been used for the pool temperature in most experiments to ensure that the fragments do not coalesce on the bottom.

110 Therefore it is assumed that the jet remains liquid during its disintegration in the water but that the droplets solidify before they hit the bottom of the vessel where they will be eventually collected to be sieved.

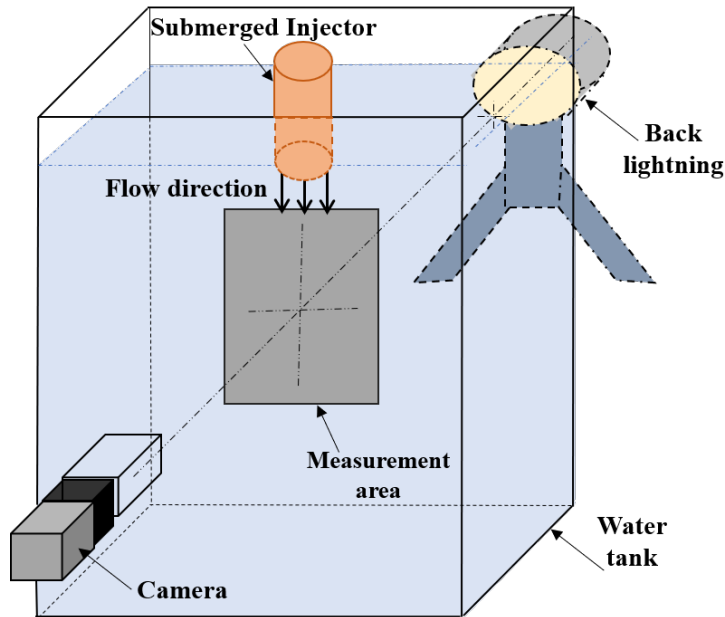


Figure 3: JaLaD experimental set-up for liquid metal jet into water.

In the present work, two measurement techniques are used to study the jet disintegration. The first technique is high speed shadowgraphy. Imaging is obtained thanks to a LED back lighting (PRIOLITE LED 400 equivalent

115

to 400W halogen light) and a phantom V701 high speed camera. The second system is simpler: it consists in a Retsch vibratory sieve shaker AS 200 which is used to separate the fragments according to their size. Each bin is thereafter weighted and the results recorded (in table 3).

120 *2.3. High Speed Shadowgraphy*

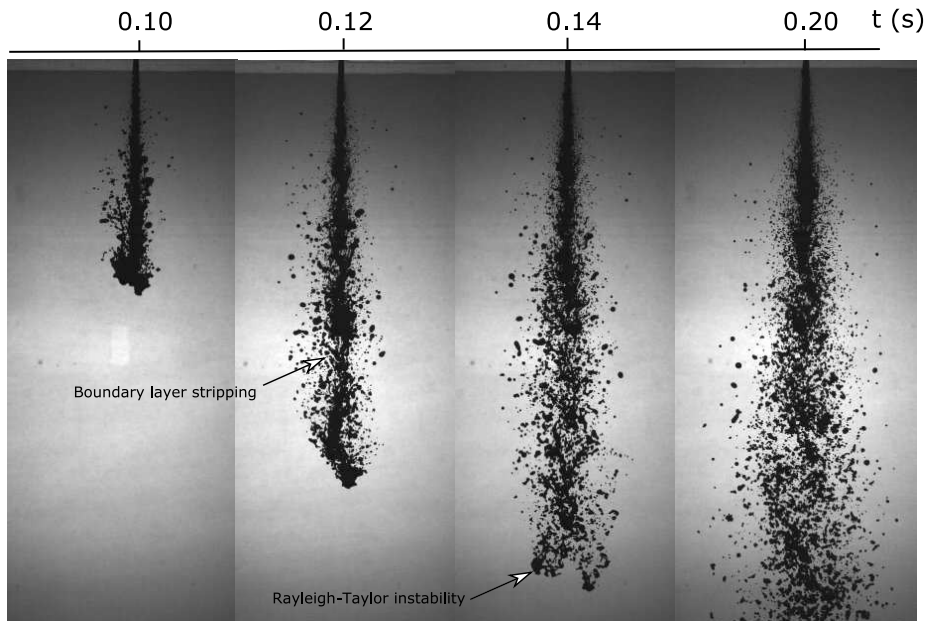


Figure 4: Shadowgraph images for D2P6 experiment. It gives insight on the possible instability mechanisms.

Figure 4 shows a sample shadowgraph. The pressure is imposed in the gas tank and measure of the tip penetration speed, obtained after image analysis, gives us an estimate of the jet velocity U_0 (*cf.* figure 5). **It gives only a crude approximation of the intial jet velocity but in present, pressure-driven experimental set-up, it is the only velocity that can be measured and we will use its value to compute the non dimensional numbers.** Table 2 indicates the four different experimental conditions for the combined shadowgraph/sieving experiments that will be studied in present work.

125

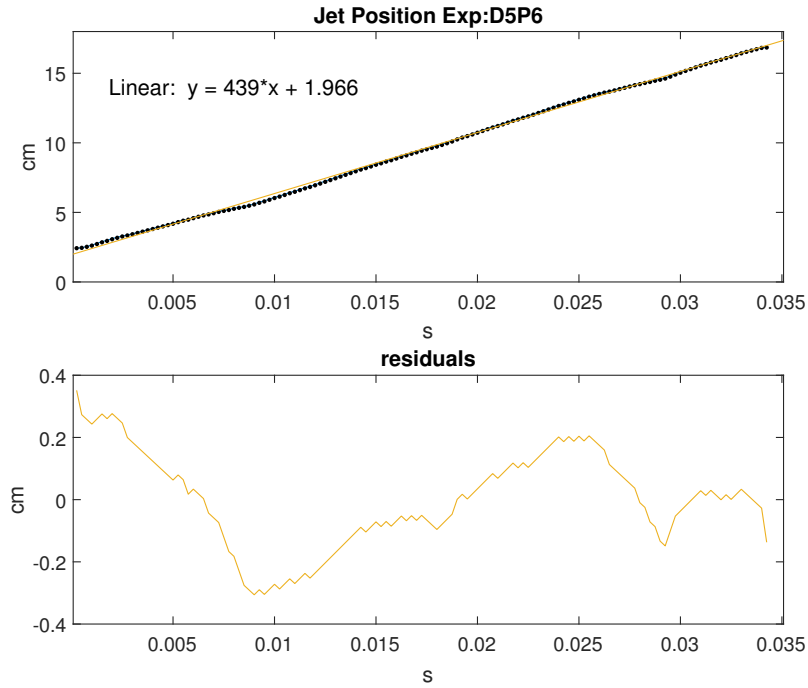


Figure 5: Jet tip position for D2P6 experiment. Computing the slope allows for determining the jet velocity (here 439 cm/s). As validation, it can be seen that the residuals show very small correlations.

130 Note that, in present analysis, shadowgraph method is used no further (as the optical density of the spray prevent for instance direct measurement of the spray PDF by image analysis).

2.4. Sieving Results

135 Table 3 indicates the result of the sieving of the solidified fragments for the four tests (summarized by their Weber number). The corresponding Mass PDF $\frac{1}{M_{tot}} \frac{dM}{d \log_{10}(D)}$ of the logarithm of the diameter $\log_{10}(D/D_0)$ is given on figure 6. It can be seen that, using the half-width height, for the lower Weber number experiments (*i.e.* $We \in [30, 40]$), most of the mass is in the range
 140 $D/D_0 \in [0.3, 1]$ while for the higher Weber number (*i.e.* $We \in [200, 300]$), most

Test	D_0	Pressure	U_0 (m/s)	We_C	Oh	Re_L	SMD/D_0
D2P6	2 mm	6 bar	2.3	26	0.0039	3697	0.47
D2P10	2 mm	10 bar	2.8	39	0.0039	4527	0.29
D5P6	5 mm	6 bar	4.4	234	0.0025	16964	0.15
D5P10	5 mm	10 bar	4.8	281	0.0025	18958	0.11

Table 2: Experimental conditions for the high-speed shadowgraphy and the sieving experiments.

We	20 μm	50 μm	100 μm	500 μm	1 mm	2 mm	Total
26.45	0.3 g	0.9 g	10.9 g	34.7 g	60.7 g	13.4 g	120.4 g
39.2	0.6 g	1.2 g	24.7 g	59.2 g	23.9 g	45.8 g	132.9 g
234	0.4 g	1.7 g	15.5 g	23.2 g	60.7 g	30.6 g	132.1 g
281	1.1 g	2.4 g	19.2 g	33.0 g	57.3 g	11.6 g	124.6 g

Table 3: Mass measurements by sieving.

of the mass is in the range $D/D_0 \in [0.1, 0.6]$.

As in [27], the values of the Sauter Mean Diameters (SMD for short, this is the diameter of the droplet that has the same surface/volume ratio as the whole cloud) given in table 2 are computed from table 3 using eq. (6).

$$SMD = \frac{1}{\sum_{i=0}^{N_s} x_i / \bar{D}_i} \quad (6)$$

145 where x_i is the mass fraction of sieve number i and $\bar{D}_i = \frac{D_i + D_{i+1}}{2}$ is the ‘‘average’’
bin sieve diameter and N_s the number of sieves used. Note that for the largest
sieve (2mm), the $i + 1^{th}$ sieve size (which does not exist and is only virtual) has
been set to $1.8 \times D_0$ to account for droplets eventually generated by Rayleigh-
Plateau instability. This has low impact on the SMD which gives more weight
150 to the small droplets however. Figure 7 shows the evolution of SMD/D_0 ratio
with Weber number. There appears to be a scaling

$$\frac{SMD}{D_0} \propto We^{-1/2} \quad (7)$$

Some other previously published results have also been included in figure 7.

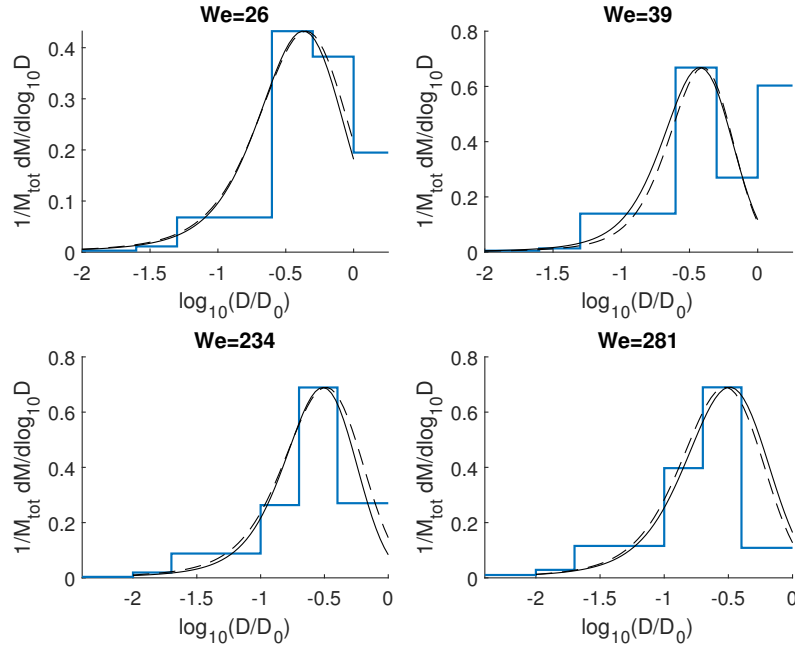


Figure 6: Mass Distribution for present experiment. Fitting of the PDF with a log-stable model is represented as a black line for the $We=281$ case. The dashed black line is the result of the model developed in the present work. Important scales (classical Kelvin-Helmholtz, Rayleigh-Taylor scale based on the jet deceleration and boundary layer "gradient" instability wavelength) are also shown for the sake of comparison.

Note that they were mostly hot experiments where some vapour was produced. Note also that this scaling seems compatible with the data published in the review [25] though the MMD is used instead of the SMD. This suggests that
 155 Rayleigh-Taylor instability (*cf.* eq. (28)) may be at play in the present fragmentation mechanism. This discussion is, however, left to next section.

3. Modelling of the experimental results

3.1. Possible instability mechanisms and relevant turbulent scales

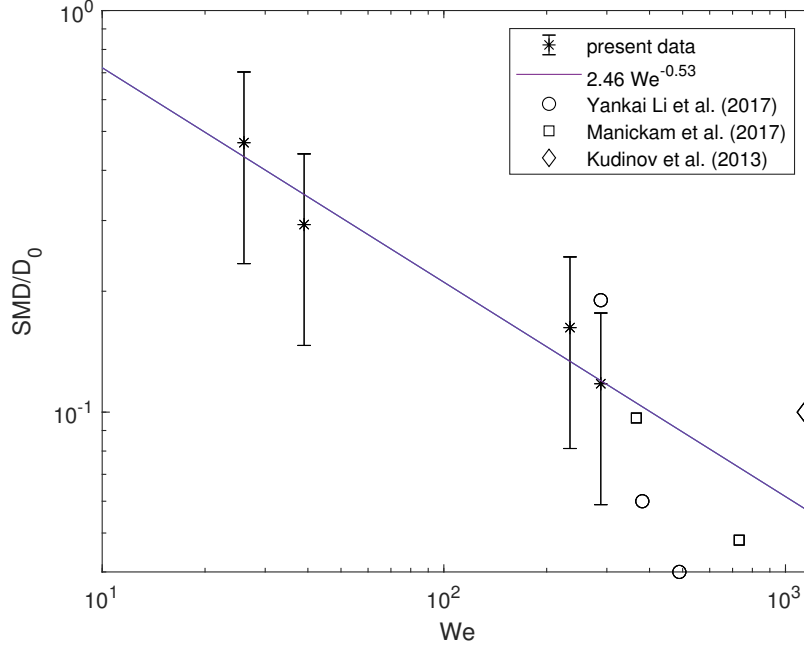


Figure 7: Sauter Mean Diameter as a function of Weber number. The line is a power-law fitting of the data

In this section, we propose to review some classical instability mechanisms that are usually associated to liquid fragmentation and compare their most amplified wavelength to the size of the fragments, hoping to be able to identify the underlying mechanisms. This is then extended to classical turbulence length scales. Therefore, the following characteristic length scales are computed: first, the (most amplified) wavelength $\lambda_{KH}^{(\gamma)}$ associated to the classical planar Kelvin-Helmholtz (*cf.* equation (8), in this classical model only surface tension is included, the two fluids are perfect, of constant density and there is a sharp velocity jump at the interface).

$$\lambda_{KH}^{(\gamma)} = \frac{3\pi\gamma(\rho_C + \rho_L)}{U_0^2 \rho_C \rho_L} \quad (8)$$

Second, the most amplified wavelength $\lambda_{RT}^{(g)}$ of Rayleigh-Taylor instability

We	$\lambda_{KH}^{(v)}/D_0$	λ_T/D_0	η/D_0	$\epsilon(m^2/s^3)$	$\lambda_{RT}^{(f)}/D_0$	$\lambda_{KH}^{(\gamma)}/D_0$
26	0.17	0.0351	1.8×10^{-3}	6083.5	0.67	0.411
39	0.15	0.0261	1.5×10^{-3}	10976	0.55	0.277
234	0.08	0.0055	4.48×10^{-4}	39753	0.23	0.047
281	0.08	0.0047	4.12×10^{-4}	55296	0.20	0.038

Table 4: Instability and turbulence characteristic length scales in the experiments

[30] is given by equation (9).

$$\lambda_{RT}^{(g)} = 2\pi \sqrt{\frac{3\gamma}{g(\rho_L - \rho_C)}} \quad (9)$$

where g is gravity acceleration. Actually g should include also the jet and the local acceleration (or deceleration) but it is not easy to determine precisely (being a second order time derivative of the jet position, it gives very noisy results) and is therefore not included here (but this idea will be used in the following).

This results in a magnitude of $\lambda_{RT}^{(g)} \approx 2.6\text{cm}$ which can be ruled out (except maybe at the tip of the jet (*cf.* figure 4 for $t = 140$ ms). **It is therefore obvious that gravity is not the main driving force of present fragmentation mechanism.**

180

Last, it is also interesting to compare these length scales with the characteristic turbulent length scale. However, to compute them, the average turbulent kinetic energy dissipation rate ϵ is needed. It is estimated as usual [33] through equation (10)

$$\epsilon \cong \frac{u'^3}{L_{int}}, \quad (10)$$

where u' represents the fluctuating velocity around the statistical average (using Reynolds decomposition) and L_{int} is the integral scale of turbulence, estimated to be of the order of magnitude of the jet diameter. This allows for the computation of Taylor's characteristic turbulent length scale and Kolmogorov's length scale through equation (11) and (12).

$$\lambda_T = \sqrt{20\nu \frac{k}{\epsilon}} \quad (11)$$

$$\eta \cong \left(\frac{\nu^3}{\varepsilon} \right)^{1/4} \quad (12)$$

190 In either eq. (10) or eq. (11), the turbulent kinetic energy k is computed assuming that $u' \approx U$ which is usually assumed true for turbulent jets.

Table 4 summarizes the results of such order of magnitude computations. Comparatively it can be seen on figure 6, that none of the proposed instability mechanisms are in the range of the half-width of the mass distribution. Likewise, 195 turbulence scales are so small that they do not seem to be connected either to the mass distribution at these Weber numbers. A new scenario will therefore be needed to explain these results.

3.2. Fitting the Mass Distribution

3.2.1. Fitting procedure

200 Figure 6 shows a fit to the mass distribution with a log-stable law:

$$\frac{1}{M_{tot}} \frac{dM}{d \log_{10}(D)} \hookrightarrow p_{\alpha}(x; \beta, \sigma, \delta) \quad (13)$$

Let us recall that Lévy stable laws are defined from their Fourier transform [34]: "A random variable X is said to have a stable distribution denoted $p_{\alpha}(x; \beta, \sigma, \delta)$ if there are real parameters $0 < \alpha \leq 2$, $0 < \sigma$, $-1 \leq \beta \leq 1$ and δ such that its *characteristic function* (*i.e.* its Fourier transform) has the following form:

$$\hat{p}_{\alpha}(k; \beta, \sigma, \delta) = \exp(ik\delta - \sigma^{\alpha}|k|^{\alpha} [1 + i(\text{sign}(k))\beta\omega(|k|, \alpha)]) \quad (14)$$

205 where

$$\omega(|k|, \alpha) = \begin{cases} \tan(\alpha\pi/2) & \text{if } \alpha \neq 1 \\ -2/\pi \log |k| & \text{if } \alpha = 1 \end{cases} \quad (15)$$

”

Simply put, the four parameters are respectively, α , the stability index governing the tail of the distribution, β the skewness parameter governing the symmetry of the law, δ the shift parameter governing the position of the maximum of the distribution and σ the scale parameter governing the width of the 210 distribution. Gaussian laws are special cases of Lévy laws with parameters:

- $\alpha = 2$,
 - β being indifferent,
 - δ being the average of the PDF
- 215 • and σ the standard deviation.

Except in the Gaussian case, Lévy laws are not square integrable, the standard deviation cannot usually be defined, hence the name scale parameter. Note that present modeling generalizes log-normal laws and not Gaussian laws as it is applied to the distribution of the logarithm of the diameter and not directly

220 to the diameter. Rimbart [16] shows theoretically that the value that should be used to describe turbulence intermittencies using log-stable laws are $\alpha = 1.7$, $\beta = -1$ (note that the distribution are said "totally skewed to the left" when $\beta = -1$). In order to keep the number of fitting parameters low, this value $\beta = -1$ has been kept fixed as it is the only value that leads to finite moments

225 of all positive orders (*e.g.* finite average diameters). Moreover the value $\alpha = 1.7$ has been related to angular momentum conservation and it has also been chosen to consider it set to this value in the present work. Therefore only the shift parameter and the scale parameters now need to be fitted. On figure 6, the shift parameter has been set so that the maximum of the log-stable distribution

230 coincides with the experimental PDF leading to the value $\delta = -0.55$ for the $We = 281$ case. Lastly the scale parameter has been varied leading to the value $\sigma = 0.24$. It therefore seems that log-stable distribution are adequate to describe the mass distribution in this intermediate Weber number liquid-liquid spray.

235 3.2.2. Comparison with previous experiments

Figures (8,9,10,11,12,13,14) show that this fitting process can also be applied to many data previously published for solidified fragments of liquid-liquid jets [21, 22, 23]. Figure 15 also shows the result of KROTOS test KA1 [35, 36, 37] that involved prototypical corium. At CEA-CADARACHE, the KROTOS facil-

240 ity allows to perform integral tests with prototypical corium, i.e. using nuclear

fuel UO_2 . The KROTOS facility consists of three parts – furnace, release channel and test sections. Tungsten crucible is filled with prototypical corium powders and then is heated up to corium liquidus temperature ($T > 2500^\circ\text{C}$) with an overheating between 100°C and 200°C . Then the crucible is released through a channel and a corium jet is formed with controlled parameter for corium jet diameter, speed, and temperature before the entrance into water. The test section is highly instrumented to follow fragmentation of the jet in conditions simulating the real reactor case conditions for the 3-phases (corium-steam-water)[35, 36]. Two kinds of tests have been performed in the frame of ICE program on KROTOS facility: premixing test and steam explosion test. This paper focuses on a premixing test performed on KROTOS facility: KROTOS KA-1. The main experimental parameters of KROTOS KA1 test were:

- corium mixture 80% UO_2 - 20% ZrO_2
- release temperature : 2710°C
- jet diameter: 30 mm
- water temperature : 58°C

The size of corium debris were between $200\ \mu\text{m}$ and $8000\ \mu\text{m}$. The main class (32%wt) was between 2000 and $4000\ \mu\text{m}$. Details of the granulometry (and other relevant parameters) of KROTOS KA1 test are given in Appendix A.

3.3. "Computing" the Mass Distribution

The goal of this section is to build a model for the computation of the scale and the shift parameter.

In order to compute the scale and shift parameter, we can consider that the shift parameter set the scale of the large fragments whose size are mainly governed by the wave instability that develops at the interface between the two fluids while the scale parameter are mainly related to the "multiplier" of the cascade model and can be related to the ratio between the first wavelength and Rayleigh-Taylor instability wavelength developing on top of the wave.

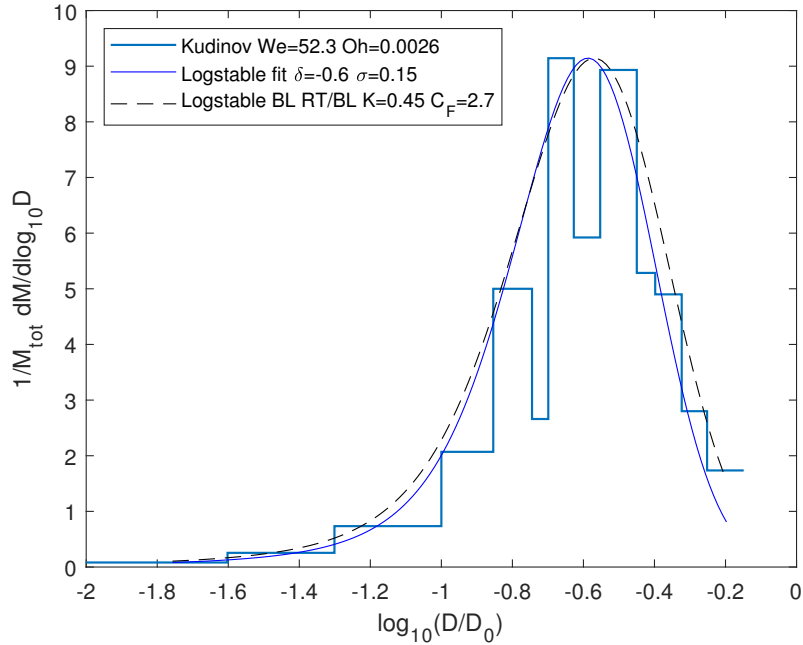


Figure 8: Mass Distribution from Kudinov *et al.* [21] DEFOR-A experiments with Bi_2O_3 - WO_3 corium simulant melt

3.3.1. Primary viscous Kelvin-Helmholtz instability

270 As has been seen in table 4, the classical Kelvin-Helmholtz model (*cf.* eq. (8)) predicts very short wavelengths that do not seem to be related to droplet sizes. We therefore propose to adapt here a model of boundary layer stripping based on a viscous Kelvin-Helmholtz (shear) instability that develop inside the Liquid phase. In order to estimate the thickness of the Liquid boundary layer,
 275 we can use a model developed by O. Girin [38]. First we assume that the boundary layer growths in the Carrier and Liquid phase are laminar and given by

$$\delta_C = K \frac{D_0}{Re_C^{*1/2}}, \quad (16)$$

$$\delta_L = K \frac{D_0}{Re_L^{*1/2}} \quad (17)$$

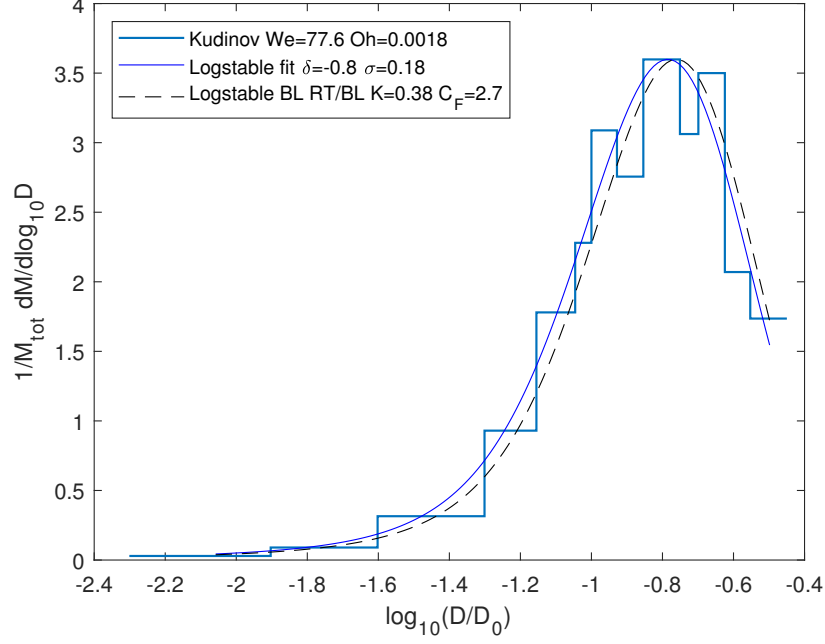


Figure 9: Mass Distribution from Kudinov *et al.* [21] DEFOR-A experiments with $\text{Bi}_2\text{O}_3\text{-WO}_3$ corium simulant melt

where K is a geometrical factor and

$$Re_L^* = \frac{\rho_L(U_L - U_S)D_0}{\mu_L}, \quad (18)$$

280

$$Re_C^* = \frac{\rho_C U_S D_0}{\mu_C}, \quad (19)$$

U_S is the surface velocity. Then using a Karman-Polhausen-Walz approach [39] using first order polynomials and using continuity of shear stress at the interface, the following relations can be established (details of the computation are given in Appendix B):

$$\delta_L = \frac{\mu_R^{2/3}}{\rho_R^{1/3}} \delta_C, \quad (20)$$

285

$$U_S = \frac{(\rho_R \mu_R)^{1/3}}{1 + (\rho_R \mu_R)^{1/3}} U_L \quad (21)$$

In the present case $\mu_R \approx 20$ and $\rho_R \approx 8$ which makes δ_C roughly one fourth of δ_L while $U_S \approx 0.84U_L$. Now the wavelength of viscous Kelvin Helmholtz instability

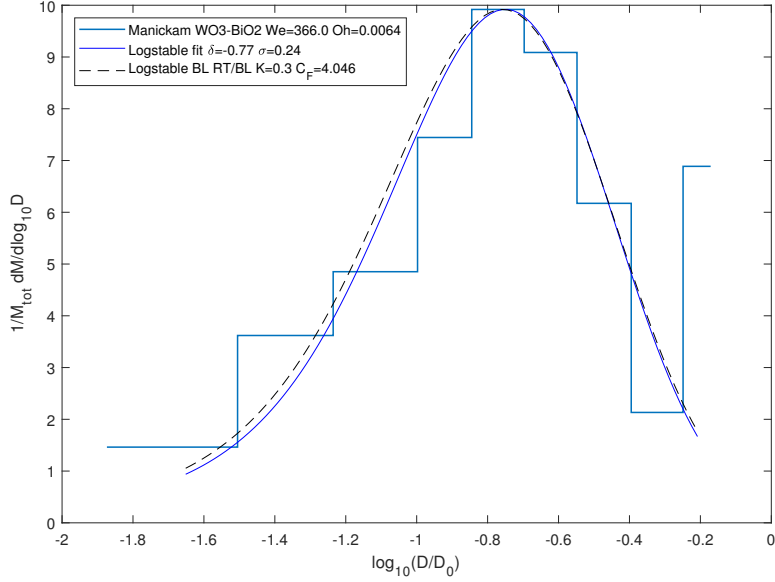


Figure 10: Mass Distribution from Manickam *et al.* [22] MISTEE Experiment with Bi_2O_3 - WO_3 corium simulant melt

is computed using $\delta_{BL} = \delta_C + \delta_L$ as the vorticity thickness in classical Rayleigh's model of planar viscous KH instability [26, 40] which gives

$$k_{KH,max}^{(v)} \delta_{BL} = 0.4. \quad (22)$$

290 where $k_{KH,max}^{(v)}$ is the most amplified wave-number of this viscous KH instability. After some simple algebra, this yields

$$\frac{\lambda_{KH}^{(v)}}{D_0} = \frac{2\pi}{0.4} \left(1 + \frac{\rho_R^{1/3}}{\mu_R^{1/3}}\right) (1 + (\rho_R \mu_R)^{1/3})^{1/2} \frac{K}{\sqrt{Re_L}}, \quad (23)$$

where $\lambda_{KH}^{(v)}$ is the most amplified wavelength of this model; and in the present case

$$\frac{\lambda_{KH}^{(v)}}{D_0} = 50.6 \frac{K}{\sqrt{Re_L}}. \quad (24)$$

Note that this can also be related to Pr. O. Girin's "gradient instability" [41].

295 **Faeth Richards, Tomotika A RAJOUTER**

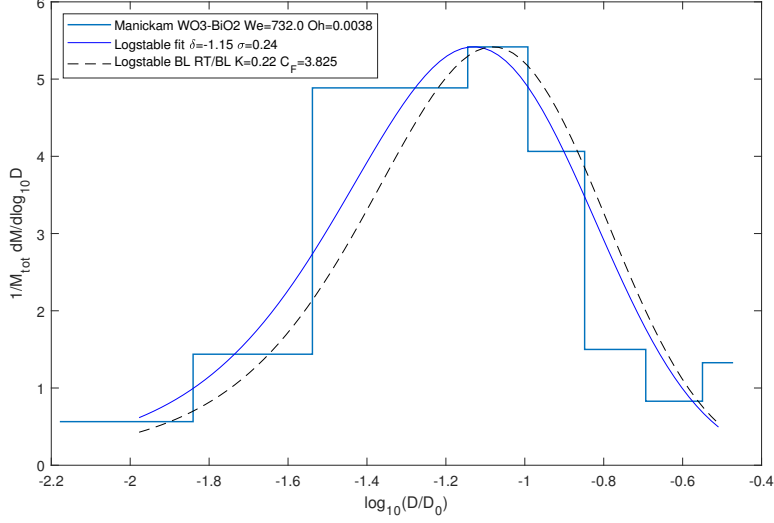


Figure 11: Mass Distribution from Manickam *et al.* [22] MISTEE Experiment with Bi_2O_3 - WO_3 corium simulant melt

3.3.2. Secondary Rayleigh-Taylor instability

In the present model, Rayleigh-Taylor instability is applied as a second step to the wave generated during the first step. We therefore consider a secondary "droplet", whose diameter will be assumed to be $D_1 \approx \lambda_{KH}^{(v)}$, and supersede its
 300 deceleration $f = dU_r/dt$ (where U_r is the relative velocity between the droplet and the surrounding fluid) to the gravity acceleration g in equation (9), using the classical approximation

$$\frac{\pi D_1^3}{6} \rho_L \frac{dU_r}{dt} \approx -\rho_C y^2 \frac{\pi D_1^2}{4} C_d U_r^2 \quad (25)$$

where y is the "droplet" extension due to its deformation by the flow (*cf.* [42] for instance) which yields

$$f \approx \frac{3}{2} \frac{\rho_C}{\rho_L} \frac{y^2}{D_1} C_d U_0^2 \quad (26)$$

305 assuming $U_r \approx U_0$. We then get

$$\frac{\lambda_{RT}^{(f)}}{D_1} \approx \pi \frac{1}{y} \sqrt{\frac{16\gamma}{C_d \rho_C U_0^2 D_1}} \quad (27)$$

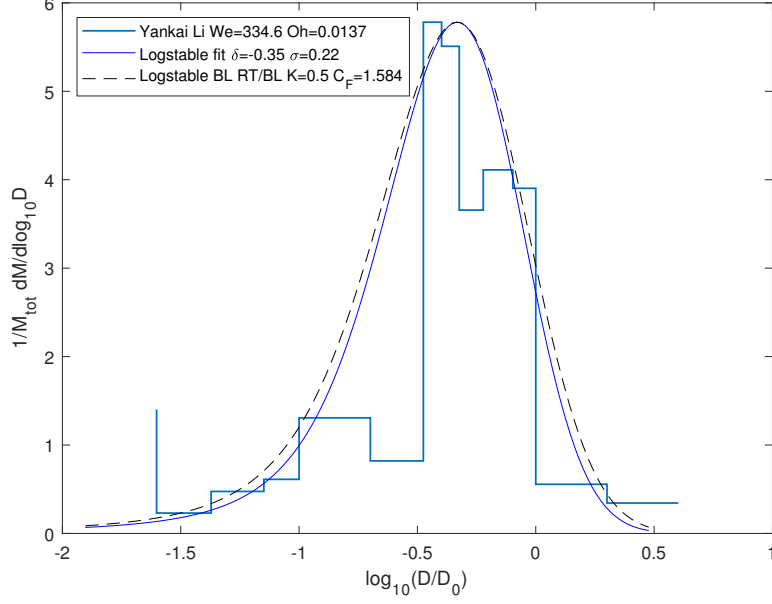


Figure 12: Mass Distribution from Yankai Li *et al.* [23] METRIC experiment with molten tin (Sn)

where $\lambda_{RT}^{(f)}$ is the Rayleigh-Taylor most amplified wavelength computing using the liquid patch deceleration f instead of gravity acceleration g . Now if we use again the approximation $D_1 \approx \lambda_{KH}^{(v)}$, one gets

$$\frac{\lambda_{RT}^{(f)}}{D_0} \approx \pi \frac{1}{y} \sqrt{\frac{8}{C_d We}} \sqrt{\frac{D_0}{\lambda_{KH}^{(v)}}} \quad (28)$$

The parameters of the log-stable distribution are therefore computed using

$$\delta = \log_{10} \frac{\lambda_{KH}^{(v)}}{D_0} \quad (29)$$

310

$$\sigma = \log_{10} \frac{\lambda_{RT}^{(f)}}{\lambda_{KH}^{(v)}} \quad (30)$$

and equations (23) and (28). Note that idea of relating some parameters of the self-similar fragmentation equation to the instability wavelengths (or the ratio of instability wavelengths), seen has the first (or second) step of the "cascade",

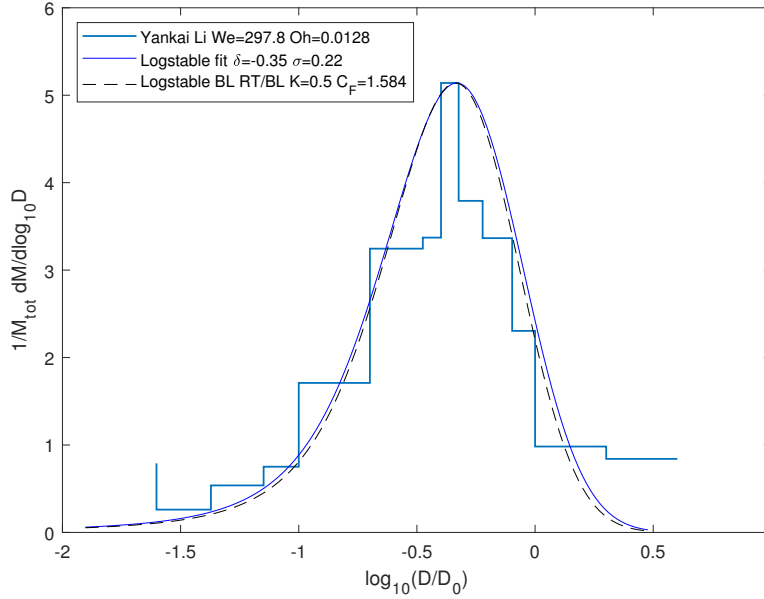


Figure 13: Mass Distribution from Yankai Li *et al.* [23] METRIC experiment with molten tin (Sn)

has been previously attempted by Gorokhovski *et al.* [8] in a numerical model,
 315 taking inspiration from the work of Varga *et al.* [11]. However, it was applied
 to the number distribution of droplet and not to their mass distribution. More-
 over, it concerned only classical Kelvin-Helmholtz and Rayleigh-Taylor instabil-
 ity (which we attempted here without success) and without cascading them.

To conclude this part, it seems that the log-stable Mass PDF that has been
 320 found as an asymptotics to the self-similar fragmentation in [6] is also valid in
 this two-step cascade model (viscous Kelvin-Helmholtz succeeded by Rayleigh-
 Taylor). Actually the self-similar fragmentation equation is also known, in
 chemical engineering, as the homogeneous fragmentation equation (see [43] for
 instance) without resorting to "cascade" arguments. This may explain why, in
 325 this rather low Weber number case, the asymptotic result may still be valid
 whereas the "cascade" is actually quite short as two steps are only required and
 high-speed video footage do not show droplets breaking up again and again.

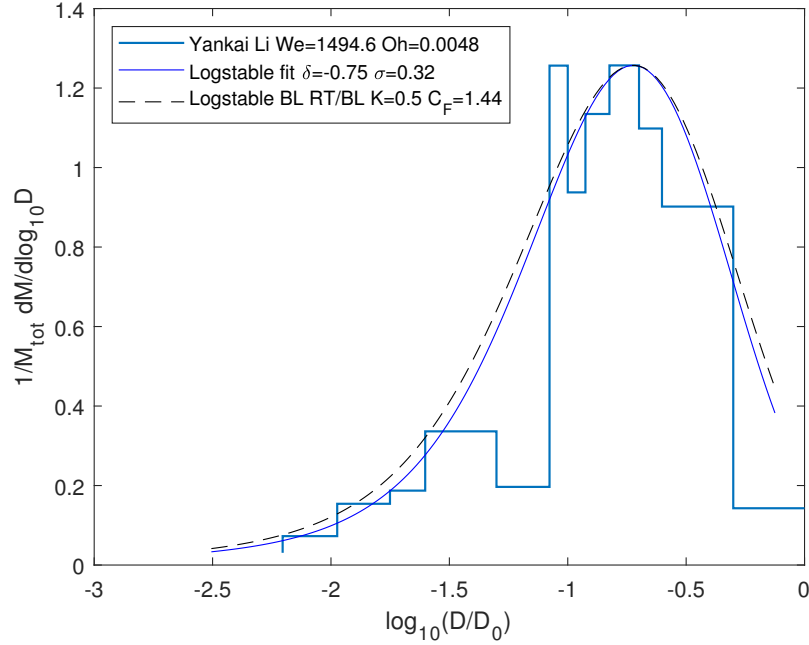


Figure 14: Mass Distribution from Yankai Li *et al.* [23] METRIC experiment with molten tin (Sn)

Actually, self-similar solutions are often observed in nature when the boundary condition (here, for the fragmentation equation: the very large and very small
 330 scales) can be somehow forgotten.

Moreover, though this part is entitled "Computing" the distribution, either the value, of y or C_d (or rather the product $C_F = C_d y^2$) and K need to be fitted in the end (though the values used are in the appropriate range *cf.* table 5). There are therefore two fitting parameters: C_F which is a friction parameter
 335 and K which is a geometrical parameter governing boundary layer development.

3.4. Comparison with previously published results

Figures (8,9,10,11,12,13,14,15) have already shown that it was possible to fit the mass distribution using log-stable laws. These figures also include as dashed line results of the present model. However some slight (and sometime

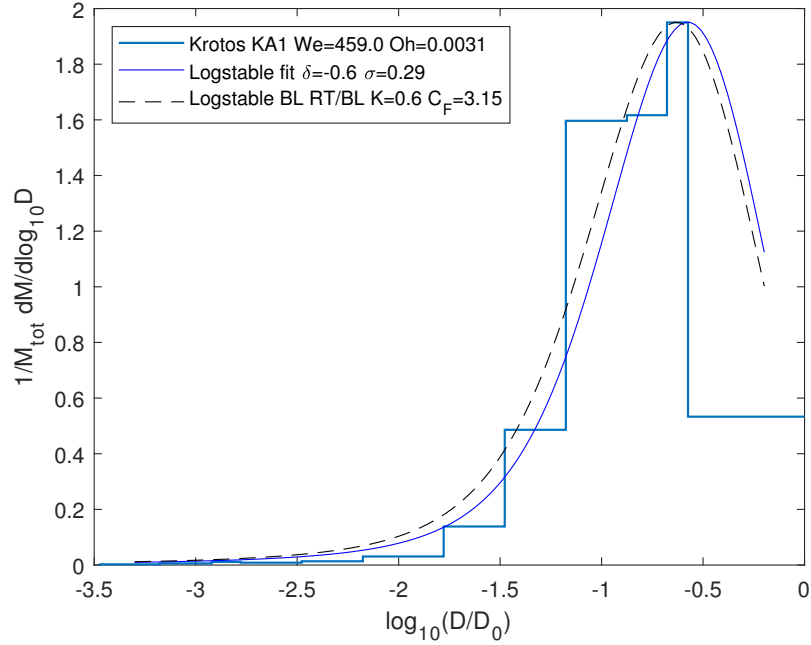


Figure 15: Mass Distribution KROTOS Test KA1 [35]

340 not that slight) fitting of the parameters C_F and K has been needed in order
 to best approximate the mass distribution of the fragments with the presented
 model. Table 5 summarizes the results of this fitting procedure. Note that the
 viscosity of the melt have also been slightly modified when deemed necessary.
 This modification is here empirical, but could be related to either solidification
 345 or oxidation mechanism that are not included in present model. This shows
 the importance of knowing the material properties precisely in order to predict
 precisely this fragmentation process.

From table 5 it can be seen that the variation of the fitting parameters
 350 are rather small with $K \approx 0.5$ and $C_F = C_d y^2$ slowly increasing from 2.3
 to 3.8 when Weber number increases. Note that this order of magnitude for
 C_F is compatible with the values reported in [44] for geophysics applications.

Name	We	Oh	$C_F = C_d y^2$	K	Viscosity	Note
D2P6	26	0.001	2.35	0.55	$\times 2$	Field's metal
D2P10	39	0.001	2.35	0.45	$\times 2$	Field's metal
Kudinov <i>et al.</i>	52	0.003	2.7	0.45	$\times 1$	Bi ₂ O ₃ -WO ₃ , low subcooling
Kudinov <i>et al.</i>	78	0.002	2.7	0.38	$\times 1$	Bi ₂ O ₃ -WO ₃ , low subcooling
D5P6	234	0.001	3.15	0.57	$\times 2$	Field's metal
D5P10	281	0.001	2.9	0.55	$\times 2$	Field's metal
Yankai Li <i>et al.</i>	298	0.013	1.58	0.50	$\times 40$	Sn, $T_m = 612^\circ\text{C}$, local vapor explosion
Yankai Li <i>et al.</i>	334	0.014	1.44	0.50	$\times 40$	Sn, $T_m = 803^\circ\text{C}$, local vapor explosion
Manickam <i>et al.</i>	366	0.006	3.15	0.35	$\times 2$	Bi ₂ O ₃ -WO ₃ , high subcooling
Krotos KA1	459	0.003	3.15	0.6	$\times 4$	UO ₂ -ZrO ₂ (80%,20%), $T_m = 2500\text{K}$
Manickam <i>et al.</i>	732	0.004	3.8	0.22	$\times 2$	Bi ₂ O ₃ -WO ₃ , high subcooling
Yankai Li <i>et al.</i>	1495	0.005	1.44	0.50	$\times 40$	Sn, $T_m = 997^\circ\text{C}$, local vapor explosion

Table 5: Fitting of the parameters C_F , K and modification of the viscosity needed to obtain log stable mass PDF close to the experiments using eq. (29) and (30). Material properties used are respectively for Bi₂O₃-WO₃, UO₂-ZrO₂ and Sn: 13.2mPas, 10mPas and 2mPas for dynamic viscosity; 6728kg/m³, 7121kg/m³, 6800kg/m³ for density and 0.18N/m, 0.8N/m, 0.57N/m for surface tension.

MISTEE Data provided by Kudinov *et al.* need very few modifications of the parameters. Moreover, the viscosity value did not need to be modified in any way, in agreement with the fact that they used an oxide melt (Bi₂O₃-WO₃) which therefore rules out oxidation. KROTOS KA1 experiments also show good agreement with present model. Uncertainty on the material properties of corium is, as usual, a problem as it is very difficult to make precise measurements on a $\approx 3000\text{K}$ melt. Two set of experimental results seems to show discrepancies that result in a modification of the fitting parameters. Experimental results of Yankai Li *et al.* used very hot liquid tin (with melt temperature ranging from 612°C to 997°C. Vaporization effect are therefore expected to be important and some localized vapor explosions have been reported by the authors. This is a known phenomenon for tin above 300°C [45, 46] when the subcooling is high (which is the case in these experiments as $\Delta T_{sub} \approx -77^\circ\text{C}$). They did not observe global vapour explosions however. Moreover, the PDF given by Yankai Li *et al.* are not very smooth and the peak of small droplets that are present on the PDF (*cf.* figures 12 and 13) can be interpreted as coming from the localized

vapour explosion that they reported. This may explain why this is the only
370 case where the viscosity was needed to be multiplied fortyfold! Note also that
it has been chosen to use the property of water at room temperature for the
carrier phase in all these analyses but in this specific case using a much smaller
density (that of the surrounding vapour) would lead to different result (in that
case there is no need to multiply the viscosity fortyfold but then, the vapour
375 density becomes the unknown parameter). Experimental results of Manickam
et al. that have been considered here, involve $\text{Bi}_2\text{O}_3\text{-WO}_3$ mixture in highly
subcooled water ($\Delta T_{sub} = -80^\circ\text{C}$). They report [22] that in this condition
the solidified glass beads can fragment yet another time when they cool down
(due to some thermal cracking). This may explain why the parameters are so
380 different in this case. Interestingly enough, the global shape of the PDF (*i.e.*
the log-stable shape) seems to be preserved even in these limit experiments.

4. Conclusion

In this work, it has been shown, by sieving solidified fragments, that for a
moderately low Weber number liquid-liquid spray, the mass distribution follows
385 a log-stable law. These laws were introduced [6] as asymptotic solution to the
self-similar fragmentation equation. This equation is usually believed to be
a mathematical translation of the recurrent "cascade" models (stemming from
Richardson's idealization of turbulence) whereas, in the present case, the cascade
seems to be far from developed: no drops seems to divide more than once or
390 twice on the video footage that we examined. Nevertheless, it seems possible
to compute all the parameters of the distribution (or rather an approximation
of their value) by considering a self-similar cascade of instability: the first step
being given by boundary layer stripping/viscous Kelvin-Helmholtz instability
and the second step being given by Rayleigh-Taylor instability. This model has
395 then been compared with previously published experiments in the field of Fuel
Coolant Interaction study, showing rather good agreement. Disagreement can
be related to either high vapor production or ternary thermal fragmentation of

the solid fragments during cooling.

Let us emphasize that corium thermophysical properties are still partially
400 known and will play an important role in the fragmentation process in the
real case of a nuclear severe accident. It could be useful to provide reliable
corium thermophysical properties such as density, surface tension and viscosity
to enhance modelling of fragmentation process.

Moreover, nothing seems to prevent application of present model to more
405 classical liquid-gas configurations; this is however, left for future considerations.

5. Declaration of Interests

The authors report no conflict of interest.

6. Acknowledgements

The work was done under the research program on nuclear safety and ra-
410 dioprotection (RSNR) and received funding from French government managed
by the National Research Agency (ANR) under Future Investments Program
(PIA), research grant No: ANR-10-RSNR-01.

Appendix A. KROTOS KA1 Data

Details can be found in references [35, 36, 37]. The following parameters are
415 used in the present modelling:

$$D_0 = 30\text{mm} \quad \rho_C = 1000\text{kg/m}^3 \quad \rho_L = 7121\text{kg/m}^3 \quad (\text{A.1})$$

$$\mu_L = 10\text{mPa.s} \quad \mu_C = 1\text{mPa.s} \quad \gamma = 0.8\text{Nm}^{-1} \quad (\text{A.2})$$

$$U_0 = 3.5\text{m/s} \quad We = 459 \quad (\text{A.3})$$

Table A.6 gives the resulting granulometry that has been measured out of these
3193.7g of corium melt.

10 μm	20 μm	36 μm	50 μm	0.1mm	0.2 mm	0.5mm	1mm	2mm	4mm	6.3mm	8mm
0.05%	0.1%	0.11%	0.17%	0.27%	0.79%	2.77%	9.72%	31.93%	21.66%	13.91%	18.52%

Table A.6: Mass measurement for KROTOS KA1. The percentage indicate the mass found in the relevant sieve size (meaning that 18.52% of the mass was in the greater than 8mm sieve).

Appendix B. Girin’s double boundary layer model

We do not need all the developments found in reference [38] here. The main
420 result stems from the equality of shear stress at the interface which reads

$$\tau_I \approx \mu_L \frac{U_L - U_S}{\delta_L} \approx \mu_C \frac{U_S}{\delta_C} \quad (\text{B.1})$$

where a first linearisation (*i.e.* first order polynomial) as been used to compute the velocity gradient. Using eq. (16) and (17) in (B.1) leads to

$$\mu_L Re_L^{*1/2} (U_L - U_S) = \mu_C Re_C^{*1/2} U_S \quad (\text{B.2})$$

But (16) and (17) also imply

$$\frac{Re_L^{*1/2}}{Re_C^{*1/2}} = \frac{\rho_L}{\rho_C} \frac{U_L - U_S}{U_S} \frac{\mu_C}{\mu_L} = \frac{\rho_R}{\mu_R} \frac{U_L - U_S}{U_S} \quad (\text{B.3})$$

Combining both (B.2) and (B.3) leads to (20) and (21).

425 References

- [1] E. Villermaux, P. Marmottant, J. Duplat, Ligament-mediated spray formation, *Phys. Rev. Lett.* 92 (2004) 074501. doi:10.1103/PhysRevLett.92.074501.
 URL <https://link.aps.org/doi/10.1103/PhysRevLett.92.074501>
- 430 [2] N. Dombrowski, W. Johns, The aerodynamic instability and disintegration of viscous liquid sheets, *Chemical Engineering Science* 18 (3) (1963) 203–214.
- [3] A. N. Kolmogorov, On the lognormal distribution law of the dimensions of particles under pulverization, in: *Doklady of the Academy of Sciences of the USSR*, Vol. 31, 1941, pp. 99–101.
435

- [4] E. Novikov, D. Dommermuth, Distribution of droplets in a turbulent spray, *Physical Review E* 56 (5) (1997) 5479.
- [5] M. Gorokhovski, V. Saveliev, Analyses of kolmogorov’s model of breakup and its application into lagrangian computation of liquid sprays under air-
440 blast atomization, *Physics of Fluids* 15 (1) (2003) 184–192.
- [6] N. Rimbart, O. Séro-Guillaume, Log-stable laws as asymptotic solutions to a fragmentation equation: application to the distribution of droplets in a high weber-number spray, *Physical Review E* 69 (5) (2004) 056316.
- [7] R. Vallon, M. Abid, F. Anselmet, Multimodal distributions of agricultural-
445 like sprays: A statistical analysis of drop population from a pressure-atomized spray, *Physical Review Fluids* 6 (2) (2021) 023604.
- [8] M. Gorokhovski, J. Jouanguy, A. Chtab-Desportes, Stochastic model of the near-to-injector spray formation assisted by a high-speed coaxial gas jet, *Fluid dynamics research* 41 (3) (2009) 035509.
- 450 [9] R. D. Reitz, Modeling atomization processes in high-pressure vaporizing sprays, *Atomisation Spray Technology* 3 (4) (1987) 309–337.
- [10] J. C. Beale, R. D. Reitz, Modeling spray atomization with the kelvin-helmholtz/rayleigh-taylor hybrid model, *Atomization and sprays* 9 (6) (1999).
- 455 [11] C. M. Varga, J. C. Lasheras, E. J. Hopfinger, Initial breakup of a small-diameter liquid jet by a high-speed gas stream, *Journal of Fluid Mechanics* 497 (2003) 405–434.
- [12] B. B. Mandelbrot, *The Fractal Geometry of Nature*, Freeman, 1982.
- [13] D. Schertzer, S. Lovejoy, Physical modeling and analysis of rain and clouds
460 by anisotropic scaling multiplicative processes, *Journal of Geophysical Research: Atmospheres* 92 (D8) (1987) 9693–9714.

- [14] S. Kida, Log-stable distribution and intermittency of turbulence, *Journal of the Physical Society of Japan* 60 (1) (1991) 5–8.
- [15] N. Rimbart, O. Séro-Guillaume, Extension of the kida law in turbulence,
465 *Comptes Rendus Mécanique* 331 (11) (2003) 775–782.
- [16] N. Rimbart, Simple model for turbulence intermittencies based on self-avoiding random vortex stretching, *Physical Review E* 81 (5) (2010) 056315.
- [17] M. Pilch, C. Erdman, Use of breakup time data and velocity history data to predict the maximum size of stable fragments for acceleration-induced
470 breakup of a liquid drop, *International Journal of Multiphase Flow* 13 (6) (1987) 741–757. doi:10.1016/0301-9322(87)90063-2.
URL <http://www.sciencedirect.com/science/article/pii/0301932287900632>
- [18] B. Gelfand, Droplet breakup phenomena in flows with velocity lag, *Progress*
475 *in energy and combustion science* 22 (3) (1996) 201–265.
- [19] Y. Abe, T. Kizu, T. Arai, H. Nariai, K. Chitose, K. Koyama, Study on thermal-hydraulic behavior during molten material and coolant interaction, *Nuclear Engineering and Design* 230 (1-3) (2004) 277–291. doi:10.1016/j.nucengdes.2003.11.032.
480 URL <http://linkinghub.elsevier.com/retrieve/pii/S0029549303003996>
- [20] Y. Abe, E. Matsuo, T. Arai, H. Nariai, K. Chitose, K. Koyama, K. Itoh, Fragmentation behavior during molten material and coolant interactions, *Nuclear Engineering and Design* 236 (14-16) (2006) 1668–1681. doi:10.1016/j.nucengdes.2006.04.008.
485 URL <http://linkinghub.elsevier.com/retrieve/pii/S0029549306003281>
- [21] P. Kudinov, A. Karbojian, C.-T. Tran, W. Villanueva, Agglomeration and

- size distribution of debris in defor-a experiments with $\text{Bi}_2\text{O}_3\text{-W}_3\text{O}_3$ corium
490 simulant melt, *Nuclear Engineering and Design* 263 (2013) 284–295.
- [22] L. Manickam, S. Bechta, W. Ma, On the fragmentation characteristics of
melt jets quenched in water, *International Journal of Multiphase Flow* 91
(2017) 262–275.
- [23] Y. Li, Z. Wang, M. Lin, M. Zhong, Y. Zhou, Y. Yang, Experimental studies
495 on breakup and fragmentation behavior of molten tin and coolant interac-
tion, *Science and Technology of Nuclear Installations* 2017 (2017).
- [24] S. Saito, Y. Abe, K. Koyama, Flow transition criteria of a liquid jet into a
liquid pool, *Nuclear engineering and design* 315 (2017) 128–143.
- [25] Y. Iwasawa, Y. Abe, Melt jet-breakup and fragmentation phenomena in
500 nuclear reactors: A review of experimental works and solidification effects,
Progress in Nuclear Energy 108 (2018) 188–203.
- [26] L. Rayleigh, On the stability, or instability, of certain fluid motions, *Proc.
London Math. Soc.* 9 (1880) 57–70.
- [27] M. Hadj-Achour, N. Rimbart, M. Gradeck, R. Meignen, Fragmentation of
505 a liquid metal droplet falling in a water pool, *Physics of Fluids* 33 (10)
(2021) 103315.
- [28] A. Amirzadeh, M. Raessi, S. Chandra, Producing molten metal droplets
smaller than the nozzle diameter using a pneumatic drop-on-demand gen-
erator, *Experimental thermal and fluid science* 47 (2013) 26–33.
- 510 [29] M. H. Achour, Fragmentation de métal liquide dans l’eau, Ph.D. thesis,
Université de Lorraine (2017).
- [30] S. Chandrasekhar, *Hydrodynamic and hydromagnetic stability*, Courier
Corporation, 2013.
- [31] A. M. Sterling, C. Sleicher, The instability of capillary jets, *Journal of Fluid
515 Mechanics* 68 (3) (1975) 477–495.

- [32] S. Lin, D. Kang, Atomization of a liquid jet, *The Physics of fluids* 30 (7) (1987) 2000–2006.
- [33] H. Tennekes, J. L. Lumley, *A First Course in Turbulence*, MIT Press, 1972.
- [34] G. Samorodnitsky, M. Taqqu, *Non-Gaussian Stable Processes: Stochastic Models with Infinite Variance*, Chapman ft Hall, London, 1994.
- 520 [35] P. Piluso, N. Cassiaut-Louis, P. Fouquart, C. Brayer, V. Tyrpek, C. Gue-
neau, T. Alpettaz, S. Gossé, Ice program: the cea experimental program
devoted to fci studies with prototypical corium, in: *The 7th European
Review Meeting on Severe Accident Research (ERMSAR-2015)*, 2015.
- 525 [36] N. Cassiaut-Louis, Réalisation de l’essai ka-1 dans le cadre
du projet rsnr-ice, Tech. Rep. RSNR-ICE/LIV/2015-12,
CEA/DEN/CAD/DTN/SMTA/LPMA (2015).
- [37] R. Meignen, P. Piluso, N. Rimbart, Outcomes of the french ice project on
fuel coolant interaction, in: *17th International Topical Meeting on Nuclear
Reactor Thermal Hydraulics, NURETH-17*, 2017, p. 16.
- 530 [38] O. G. Girin, Model of the fuel jet primary atomization and aerodynamics of
spray formation at high-pressure injection in a diesel engine, *Atomization
and Sprays* 28 (3) (2018).
- [39] H. Schlichting, K. Gersten, *Boundary layer theory*, Springer, 1961.
- 535 [40] F. Charru, *Instabilités hydrodynamiques*, EDP sciences, 2012.
- [41] O. Girin, Hydrodynamic instability and regimes of fragmentation of drops,
Journal of engineering physics 48 (5) (1985) 560–564.
- [42] N. Rimbart, S. C. Escobar, R. Meignen, M. Hadj-Achour, M. Gradeck,
Spheroidal droplet deformation, oscillation and breakup in uniform outer
540 flow, *Journal of Fluid Mechanics* 904 (2020).

- [43] M. Kostoglou, Exact self-similar solutions to the fragmentation equation with homogeneous discrete kernel, *Physica A: Statistical Mechanics and its Applications* 320 (2003) 84–96.
- [44] B. Qaddah, J. Monteux, V. Clesi, M. A. Bouhifd, M. Le Bars, Dynamics and stability of an iron drop falling in a magma ocean, *Physics of the Earth and Planetary Interiors* 289 (2019) 75–89.
- [45] T. Dullforce, D. Buchanan, R. Peckover, Self-triggering of small-scale fuel-coolant interactions: I. experiments, *Journal of Physics D: Applied Physics* 9 (9) (1976) 1295.
- [46] K. Matsumura, H. Nariai, Self-triggering mechanism of vapor explosions for a molten tin and water system, *Journal of nuclear science and technology* 33 (4) (1996) 298–306.